PAPER

Check for updates

Inhibiting metal-inward diffusion-induced degradation through strong chemical coordination toward stable and efficient inverted perovskite solar cells†

Jiabao Yang,[a] Qi Cao,[a] Tong Wang,[a] Bowen Yang,[bc] Xingyu Pu,[a] Yixin Zhang,[a] Hui Chen,[a] Ilhom Tojiboyev, [d] Yuke Li, [e] Lioz Etgar, [f] Xuanhua Li *[a] and Anders Hagfeldt [bc]

The inward diffusion of metal electrodes is one of the main reasons for the deterioration of the long-term device stability of perovskite solar cells (PSCs). Thus, herein, we adopt a simple additive engineering strategy to modify the barrier material bathocuproine (BCP) with 1,3,5-triazine-2,4,6-trithiol trisodium salt (TTTS). Different from the traditional physical blocking strategies, TTTS could prevent the metal electrodes (*e.g.*, gold, silver, and copper) from diffusing inward through the strong chemical coordination between TTTS and the metal electrode. The TTTS additive also improved the conductivity and band structure of BCP, thus enhancing the ability of BCP to extract electrons from the perovskite layer to the electrode. Consequently, the inverted device modified with TTTS exhibited a high efficiency of 22.59%, which is among the highest efficiencies reported to date for inverted PSCs. More importantly, it showed excellent operational, ambient, and thermal stability. The target device maintained its initial efficiency with no loss under continuous one-sun illumination at maximum power point tracking after 1000 h (the champion device), 91% in air (50% ± 5% RH) for 5000 h, and 93% after heating at 85 °C for 1500 h (average efficiency from ten devices).

Broader context
Perovskite solar cells (PSCs) have rapidly developed in the past decade due to their excellent optoelectronic properties. The photoelectric conversion efficiency (PCE) of inverted PSCs has quickly increased to 23%, which is approaching that of regular-structured devices. However, long-term stability is still the main obstacle restricting their commercialization. Although numerous physical separation barriers have been proven to effectively enhance the device stability, they do not satisfy operational stability at high efficiency. In this context, a chemical barrier strategy using a triazine salt chelating agent to coordinate the metal electrode achieves inhibition of its inward diffusion and excellent operational, ambient, and thermal stabilities. Our work provides a new strategy to improve the device efficiency and stability, thus hopefully can be applied for the commercialization of PSCs.

a State Key Laboratory of Solidification Processing, Center for Nano Energy Materials, School of Materials Science and Engineering, Northwestern Polytechnical University, Xi'an 710072, People's Republic of China. E-mail: lixh32@nwpu.edu.cn

b Department of Chemistry-Ångström Laboratory, Uppsala University, SE-75120 Uppsala, Sweden

c Laboratory of Photomolecular Science, Institute of Chemical Sciences and Engineering, School of Basic Sciences, Ecole Polytechnique Fédérale de Lausanne, CH-1015 Lausanne, Switzerland

d Institute Ion – Plasma and Laser Technologies, Uzbekistan Academy of Sciences, 100125, Durmon yuli 33 Tashkent, Uzbekistan

e Department of Chemistry and Centre for Scientific Modeling and Computation, Chinese University of Hong Kong, Shatin, Hong Kong, China

f Institute of Chemistry, Casali Center for Applied Chemistry, The Hebrew University of Jerusalem, Jerusalem 91904, Israel

† Electronic supplementary information (ESI) available. See DOI: **https://doi.org/10.1039/d1ee04022g**

1. Introduction

The power conversion efficiency (PCE) of perovskite solar cells (PSCs) has been rapidly improving in the past decade owing to their tunable bandgap,[1–3] high absorption coefficient,[4–6] high charge mobility,[7,8] low exciton binding energy,[9–11] long carrier diffusion length,[12–14] simple process[15,16] and low manufacturing cost.[17–19] The PCE of normal (n–i–p) PSCs exceeds 25.5%,[20] while that of inverted PSCs has reached 23.0%.[21] Although the PCE of PSCs is impressive, their poor stability has become a bottleneck, restricting their commercialization.[22–24]

The inward diffusion of the metal electrode has been proven to be one of the critical issues that deteriorates the device

2154 | *Energy Environ. Sci.*, 2022, **15**, 2154–2163

This journal is © The Royal Society of Chemistry 2022

stability.[25,26] As reported by Grätzel et al., a considerable amount of Au diffused inward to the perovskite region through the charge transport layer (CTL) when the temperature of thermal aging exceeded 70 °C.[27] Boyd et al. reported that the metal electrode migrated into the active layer and degraded the photoelectric performance and stability of PSCs after accelerated aging.[28] Ming et al. conducted first-principles calculations on the formation energetics and diffusion dynamics in the perovskite layer for common metals. They showed that many metals can diffuse into the perovskite and introduce deep-level defects, consequently promoting the degradation of the perovskite.[29] Thus far, physical barriers are widely employed to block the inward diffusion of the metal electrode via interface engineering at the interface of perovskite/CTL or CTL/electrode. Liu et al. reported that the diffusion of the metal electrodes could be inhibited by a surface patch constructed via the introduction of methimazole (MMI) to form an MMI–PbI$_2$ complex at the perovskite/CTL interface.[30] The target device maintained almost 80% of its initial efficiency after one-sun continuous illumination for 672 h. Wu et al. reported that the Bi at the CTL/electrode interface could protect the metal from migrating to the perovskite layer for 500 h in N$_2$.[31] In addition, Cr,[32] Al$_2$O$_3$,[33] MoO$_x$,[34] ZnO[35] and AgAl[36] layers were also employed as physical barriers at the CTL/electrode interface.[37,38] However, the metal atoms tend to diffuse through these physical separation barriers under long-term light or heat stresses, which is not beneficial to the perdurable stability of the device and high efficiency.

Herein, we introduced the 1,3,5-triazine-2,4,6-trithiol trisodium salt (TTTS) in the common barrier material bathocuproine (BCP) via a simple additive engineering strategy to block the diffusion of the metal electrode via strong chemical coordination, as shown in Fig. 1(a). TTTS is a chelating agent to precipitate heavy metals because it contains three sulfur ions with very strong lone pair electrons, where it binds the elemental forms of metals. In our studies, TTTS could coordinate with common metals electrode, such as gold (Au), silver (Ag) and copper (Cu). Different from the physical blocking strategies, TTTS could prevent the metal electrode from diffusing inward via the interaction between the metal electrode and its sulfur (S) atoms. In addition, the TTTS additive improved the conductivity and optimized the band structure of the BCP layer for more efficient charge extraction. Consequently, the modified PSCs achieved a champion PCE of 22.59% and excellent operational, ambient, and thermal stability. The encapsulated champion devices with modified BCP layer exhibited almost no loss in their initial power output after continuous one-sun illumination at 45 °C and the maximum power point tracking of 1000 h. In addition, the unencapsulated device also showed 91% (average PCE from ten devices) ambient stability when tested at 50% ± 5% relative humidity (RH) and 25 °C in air for 5000 h and 93% (average PCE from ten devices) thermal stability when tested at 85 °C in N$_2$ for 1500 h. Thus, this work provides an effective strategy to simultaneously block the inward diffusion of the metal electrode and enhance the device efficiency.
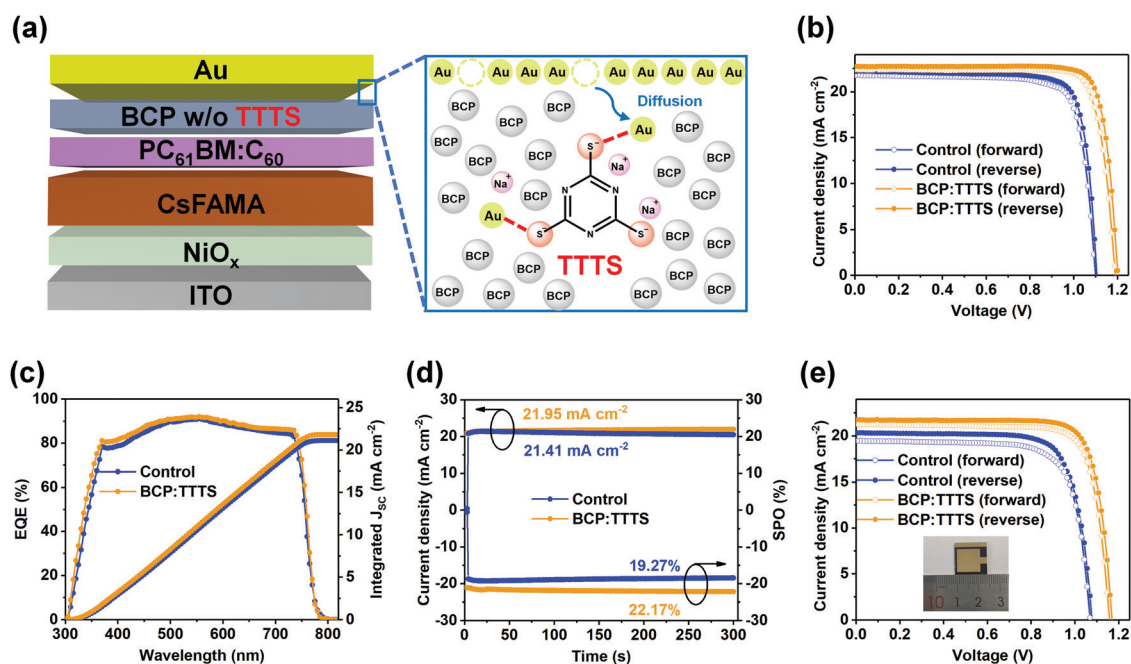

Fig. 1 Device structure and photoelectric performance of PSCs. (a) Device structure and schematic of the BCP layer with TTTS. (b) J–V curves at different scan directions of the champion devices without or with TTTS. The scan rate is 0.1 V s^{-1}. (c) EQE spectra and the corresponding integrated J_{SC} of the control and TTTS-modified devices. (d) Steady-state photocurrent and SPO of the control and BCP:TTTS devices (MPP is 0.90 and 1.01 eV, respectively). (e) J–V characterization of the large-area devices (1 cm^2) without or with TTTS. The scan rate is 0.1 V s^{-1}. The inset is a photo of the large-area device.

2. Results and discussion

The structure of the prepared PSCs is ITO/NiO$_x$ (20 nm)/perovskite (about 550 nm, denoted as CsFAMA)/PCBM:C$_{60}$ (about 46 nm)/BCP without or with TTTS (10 nm)/Au (100 nm) (Cs is caesium, FA is formamidinium, MA is methylammonium, PCBM is [6,6]-phenyl-C61-butyric acid methyl ester, and ITO is indium tin oxide), as shown in Fig. 1(a). The TTTS molecule was introduced in the BCP layer by blending BCP and TTTS as a mixed layer (termed BCP:TTTS). First, we investigated the device photoelectric performance via J–V curves. The device was optimized using different concentrations of TTTS in the BCP layer (Fig. S1, ESI†) and the detailed photoelectric parameters are recorded in Table S1 (ESI†) (the scan rate is 0.1 V s^{-1}). The optimal concentration of the TTTS additive is 0.05 mg mL^{-1}, and the corresponding device is denoted as BCP:TTTS device. The reverse and forward scanning curves and the corresponding detailed parameters are recorded in Fig. 1(b) and Table 1, respectively. The BCP:TTTS device displayed an increase in PCE from 19.93% (19.04) to 22.59% (21.88) due to the increase in the open-circuit voltage (V_{OC}) from 1.11 (1.10) V to 1.20 (1.19) V, J_{SC} from 22.24 (21.73) mA cm^{-2} to 22.73 (22.36) mA cm^{-2} and fill factor (FF) from 80.74% (79.67) to 82.84% (82.24) in the reverse (forward) direction. The PCE of the control device was consistent with the previous result[39] and that of the BCP:TTTS device is among the highest for inverted devices reported to date. In addition, the BCP:TTTS device showed superior reproducibility (see the device statistics in Fig. S2, ESI†).

We measured the external quantum efficiency (EQE) of the control and BCP:TTTS devices, as shown in Fig. 1(c). Compared with the control device, a higher EQE in the entire wavelength region for the BCP:TTTS device was observed. The integrated J_{SC} values are consistent with the J–V curves for the control (21.12 mA cm^{-2}) and BCP:TTTS (21.81 mA cm^{-2}) devices. In addition, the steady-state photocurrent and stabilized power output (SPO) of the devices were measured at the maximum power point (i.e., MPP, 0.90 and 1.01 V for the control and BCP:TTTS devices, respectively), as shown in Fig. 1(d). Compared with the slightly decreased SPO for the control device, the higher and more stable SPO for the BCP:TTTS device is satisfactory. In addition, we prepared an upscaled device with an active area of 1 cm^2 and obtained a PCE of 20.21% via the blade coating and anti-immersion method, revealing that our strategy is feasible for large-area devices (Fig. 1(e) and Table S2, ESI†).

We further investigated the optical and electrical properties of the BCP:TTTS device. The absorption of both the control and BCP:TTTS devices was similar (Fig. S3, ESI†). In addition, the introduction of TTTS in the BCP film had little effect on the morphology of the BCP layer, which was confirmed by the SEM images (Fig. S4, ESI†), AFM images (Fig. S5, ESI†), and XPS spectra (Fig. S6, ESI†). We further studied the influence of TTTS on the electrical properties of the BCP film. The characterization of the conductivity with the structures of ITO/BCP without or with TTTS/Au is shown in Fig. 2(a). The conductivity of the BCP film increased from 0.71 × 10^{-5} to 1.09 × 10^{-5} S cm^{-1} after modification with TTTS, which reveals its electron extraction capability.[40] Transient photocurrent (TPC) measurement was also employed to characterize the carrier extraction and collection efficiency of an entire device (Fig. 2(b)). The TPC decay time for the BCP:TTTS device (0.16 μs) was shorter than that of the control device (0.30 μs), indicating its better carrier extraction and collection after TTTS modification.[41] The charge recombination and carrier lifetime were characterized by the transient photovoltage (TPV) decay time. The TPV measurement showed an enhancement in the carrier lifetime from 631.61 to 1092.70 μs after TTTS modification, indicating that the TTTS additive is beneficial to reduce charge recombination and enhance carrier transport (Fig. 2(c)).

We calculated the electronic energy level diagram (Fig. 2(d)) using the Tauc plots of $(\alpha h\nu)^2$ versus $h\nu$ (Fig. S7, ESI†) and ultraviolet photoelectron spectroscopy (UPS) (Fig. 2(e)) to inspect the mechanism of the excellent electrical properties of the films. The band gaps of the BCP and BCP:TTTS films were 3.62 and 3.59 eV, respectively. The calculated Fermi level (E_F) exhibited almost no change after TTTS modification, which was 4.09 and 4.06 eV for the BCP and BCP:TTTS films, respectively. Compared with the BCP film, the conduction band minimum (CBM) of the BCP:TTTS film shifted to a deeper level by about 0.1 eV accompanied by an increase in electron affinity. Therefore, there is narrower energy gap between E_F and CBM ($\Delta E_C = E_{CBM} - E_F$) when BCP is coated on top of the PCBM:C$_{60}$ layer, which indicates a lower electronic barrier and higher electron extraction ability, as shown in Fig. 2(f).[42] In addition, the wider energy gap between E_F and the valence band maximum (VBM) ($\Delta E_V = E_F - E_{VBM}$) reveals higher hole-blocking ability.[43] A lower electronic barrier and higher hole-blocking ability are expected to result in better electron extraction. The BCP:TTTS device also displayed a smaller series resistance (R_s) and larger shunt resistance (R_{sh}), as shown in Table 1, which was confirmed by electrochemical impedance spectroscopy (EIS) (Fig. S8, ESI†) and dark J–V characterization (Fig. S9, ESI†). Overall, the improved V_{OC} is likely attributed to the better band alignment and reduced charge recombination; the

Table 1 The photovoltaic parameters of the devices without and with TTTS in the forward and reverse scan directions. The scan rate is 0.1 V s^{-1}

Device (mg mL^{-1})		V_{OC} (V)	J_{SC} (mA cm^{-2})	FF (%)	PCE (%)	R_s (Ω cm^2)	R_{sh} (Ω cm^2)
Control	F[a]	1.10 (1.10 ± 0.02)	21.73 (20.71 ± 0.26)	79.67 (78.86 ± 0.47)	19.04 (18.12 ± 0.58)	8.54	2601
	R[b]	1.11 (1.10 ± 0.02)	22.24 (21.73 ± 0.24)	80.74 (79.95 ± 0.42)	19.93 (19.09 ± 0.54)		
0.05	F[a]	1.19 (1.19 ± 0.01)	22.36 (22.01 ± 0.22)	82.24 (81.78 ± 0.37)	21.88 (21.05 ± 0.36)	2.03	18824
	R[b]	1.20 (1.20 ± 0.01)	22.73 (22.42 ± 0.19)	82.84 (82.41 ± 0.35)	22.59 (21.87 ± 0.33)		

[a] The forward scan direction. [b] The reverse scan direction.

2156 | *Energy Environ. Sci.*, 2022, **15**, 2154–2163

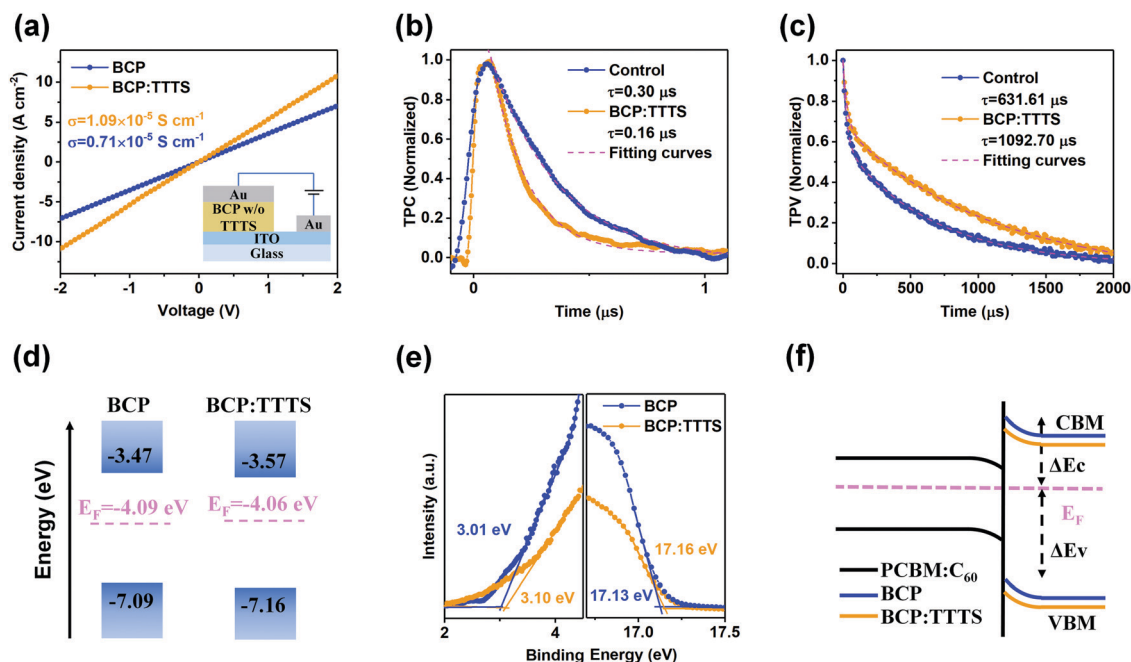This journal is © The Royal Society of Chemistry 2022

Fig. 2 Electrical characterization of devices. (a) Conductivity measurements of BCP films without and with TTTS. The inset is the device structure with ITO/BCP without and with the TTTS/Au design. (b) TPC and (c) TPV decay characteristics of the control and BCP:TTTS devices. The fitting curves were obtained from a bi-exponential decay function. (d) Electronic energy level diagram of BCP films without and with TTTS. (e) UPS spectra of BCP and BCP:TTTS films. (f) Band diagram after the BCP layer or BCP:TTTS layer is spin-coated over the PCBM:C_{60} layer.

increased J_{SC} of the BCP:TTTS devices should be attributed to the enhanced carrier extraction and transport; and the increment in FF mainly stems from the decreased R_s and increased R_{sh} (Fig. S8 and S9, ESI† and Table 1).

In addition to the excellent PCE, we continued to monitor the operational, ambient, and thermal stabilities of the devices without and with TTTS (relevant parameters of aging experiments are given in Tables S3–S5, ESI†). Fig. 3(a) displays the operational stability of the encapsulated champion devices soaked in one-sun continuous illumination at 45 °C to track MPP. The optimized device exhibited no loss in its initial SPO after 1000 h, while the control device exhibited 55% loss after 630 h. We also studied the ambient stability at 25 °C and 50% ± 5% relative humidity (RH), as shown in Fig. 3(b). The unencapsulated BCP:TTTS device maintained 91% (average PCE from ten devices) of its initial PCE after 5000 h, while the control device just retained 64% after 2100 h. Fig. 3(c) shows the thermal stability test with the unencapsulated devices at 85 °C for 1500 h in a N_2-filled glovebox. The BCP: TTTS device maintained 93% of its PCE (average PCE from ten devices) after 1500 h, whereas the control device only retained 62% of its PCE after 800 h.

We investigated the origin of the stability enhancement after TTTS modification. First, Fourier transform infrared spectroscopy (FTIR) (Fig. S10, ESI†) and X-ray photoelectron spectroscopy (XPS) (Fig. 4(a) and (b) and Fig. S11, ESI†) were performed to investigate the interaction between TTTS and the Au electrode (note: an ~10 nm thin Au film was thermally deposited on top of the TTTS, BCP or BCP:TTTS film to obtain better FTIR and XPS information). The peak at 845.2 cm^{-1} in the FTIR spectrum of the TTTS film is assigned to the stretching

vibration peak of C–S, which is blue-shifted to a higher wave-number at 850.7 cm^{-1} after the thermal deposition of Au. This result indicates that the S in TTTS may interact with Au. We further obtained evidence for the molecular interactions between TTTS and Au *via* XPS. It is observed that the two main peaks of Au 4f located at 87.8 and 84.1 eV for the BCP/Au film shifted towards a higher binding energy after the incorporation of TTTS (corresponding to 88.0 and 84.3 eV for the BCP:TTTS/Au film), respectively. In addition, a new doublet appeared at 88.9 and 85.1 eV in the Au 4f XPS spectra after deconvolution for the BCP:TTTS/Au film, which should be attributed to the S–Au bond.[44] Meanwhile, we found that the two main peaks of S 2p from the BCP:TTTS/Au film shifted towards lower binding eneries at 163.0 and 161.9 eV compared with that of the pure TTTS film (163.2 and 162.0 eV), respectively (Fig. 4(b)). The weaker doublet at 162.6 and 161.6 eV suggests the formation of an S–Au bond, indicating the strong chemical coordination interaction between TTTS and Au.[45] It should be noted that we did not observe strong interaction between the N atoms in TTTS and Au because the lone pair of the N atoms contributes to the conjugation system of the triazine ring (see Fig. S11, ESI† and detailed discussion).

The strong interaction between TTTS and Au enabled the more conformal deposition of Au. To study the effect of TTTS on the buried surface of the Au electrode, we obtained the scanning electron microscopy (SEM) images of the BCP and BCP:TTTS films with thin Au film (~20 nm). As shown in Fig. 4(c), an intermittent Au surface is observed when Au was directly deposited on top of the BCP film. After the incorporation of TTTS additive into the BCP film, interestingly, the Au film became smoother and more uniform (Fig. 4(d)), which
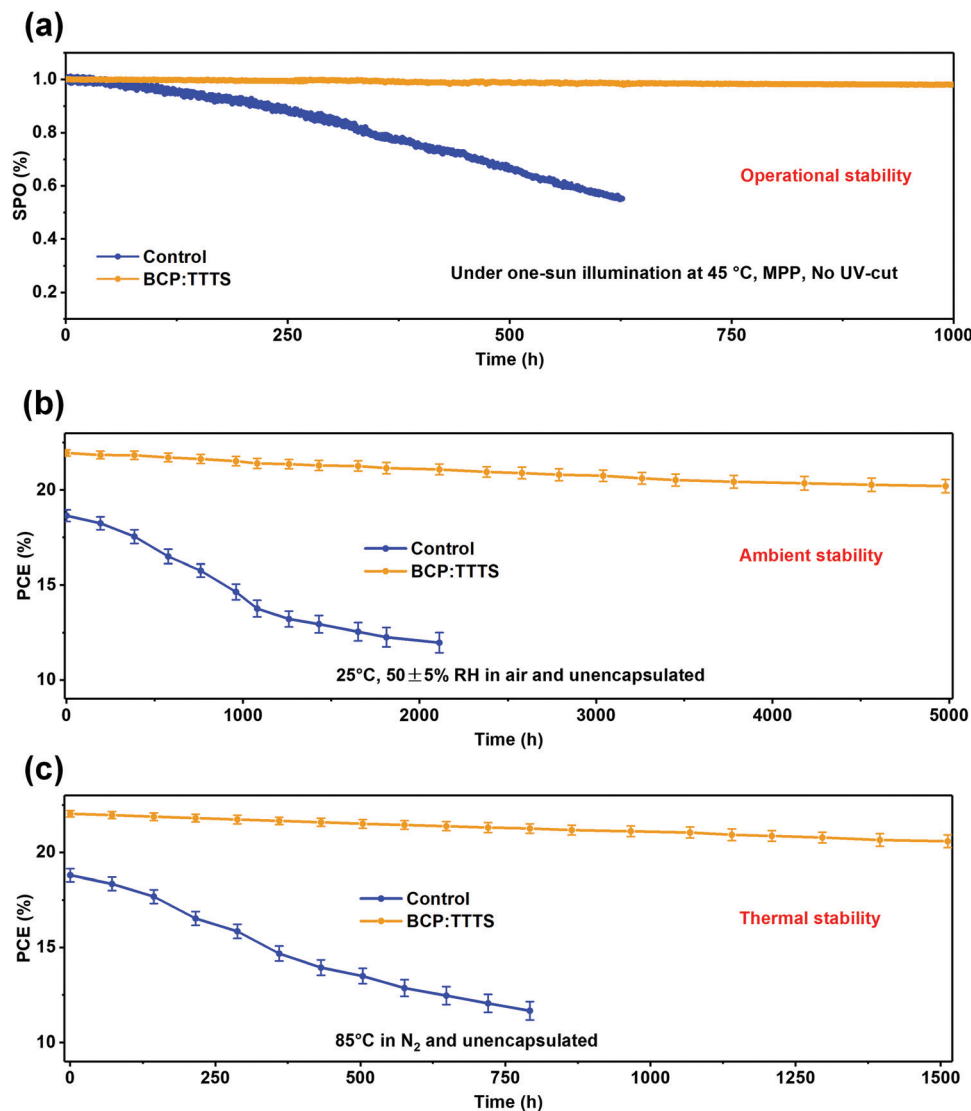
Fig. 3 Stability characterization of the control and BCP:TTTS devices. (a) Operational stability test of encapsulated devices under one-sun illumination without UV (ultraviolet) filter at 45 °C to track the MPP. The SPO trace is the degradation of a single champion device for the control and BCP:TTTS devices. (b) Ambient stability test of unencapsulated devices in air (25 °C, 50 ± 5% RH). (c) Thermal stability test of unencapsulated devices at 85 °C in an N_2-filled glovebox. The average PCE and standard error were calculated from ten devices.

should be attributed to the interaction between TTTS and Au to immobilize the Au atoms and effectively improve the Au growth kinetics.[46,47] Atomic force microscopy (AFM) images also confirm the smaller root-mean-square (RMS) surface roughness of the BCP:TTTS/Au film (4.15 nm) compared to that of the BCP/Au film (4.52 nm) (Fig. 4(e) and (f), respectively). The smooth and conformal Au film is favorable for the extraction of electrons from the electron transport layer (ETL) to the Au electrode.[48]

We performed conductive-atomic force microscopy (C-AFM) to explore the impact of Au migration on the perovskite films.[49] As shown in Fig. 5(a), the ETL and Au electrode coating on the perovskite films were stripped after continuous heating at 85 °C after 0, 100, 200 and 300 h, respectively. All the C-AFM images were obtained under an applied bias of 1 V on the perovskite

films (Fig. 5(b)). In the case of the perovskite film based on the BCP layer, the current signal gradually increased with an increase in the heating time. A clear current signal appeared at the grain boundary of the control perovskite film after continuous heating for 300 h compared with the corresponding topography (Fig. S12, ESI†), indicating a significantly enhanced transmission pathway in the perovskite film, which is attributed to the migrated Au.[50] On the contrary, there was no obvious current intensity change for the perovskite film based on the BCP:TTTS layer. The current of the perovskite film did not increase significantly even after 300 h of heating, indicating the effective blocking ability of TTTS on Au. The diffused Au on the perovskite film was further observed by SEM imaging and energy dispersive X-ray (EDX) mapping, as shown in Fig. S13 (ESI†).
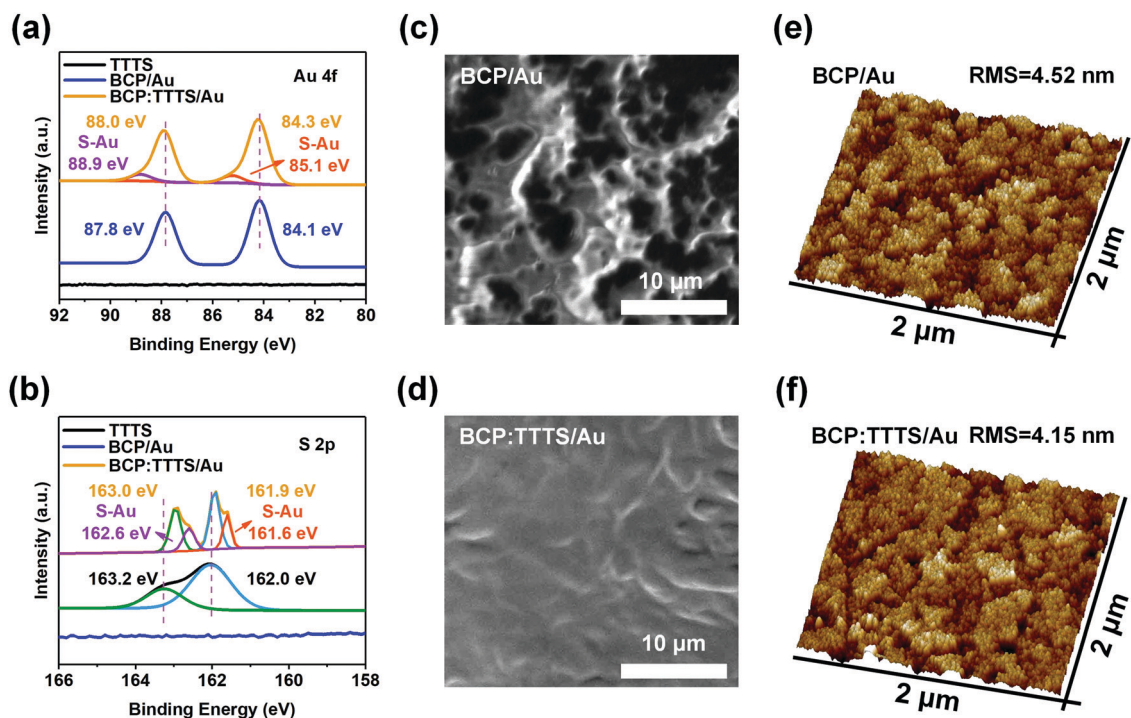
Fig. 4 Effect of TTTS on the Au electrode. (a) Au 4f and (b) S 2p XPS spectra of TTTS, BCP/Au and BCP:TTTS/Au films. SEM images of (c) the BCP/Au film and (d) BCP:TTTS/Au film. AFM images of (e) BCP/Au film and (f) BCP:TTTS/Au film.
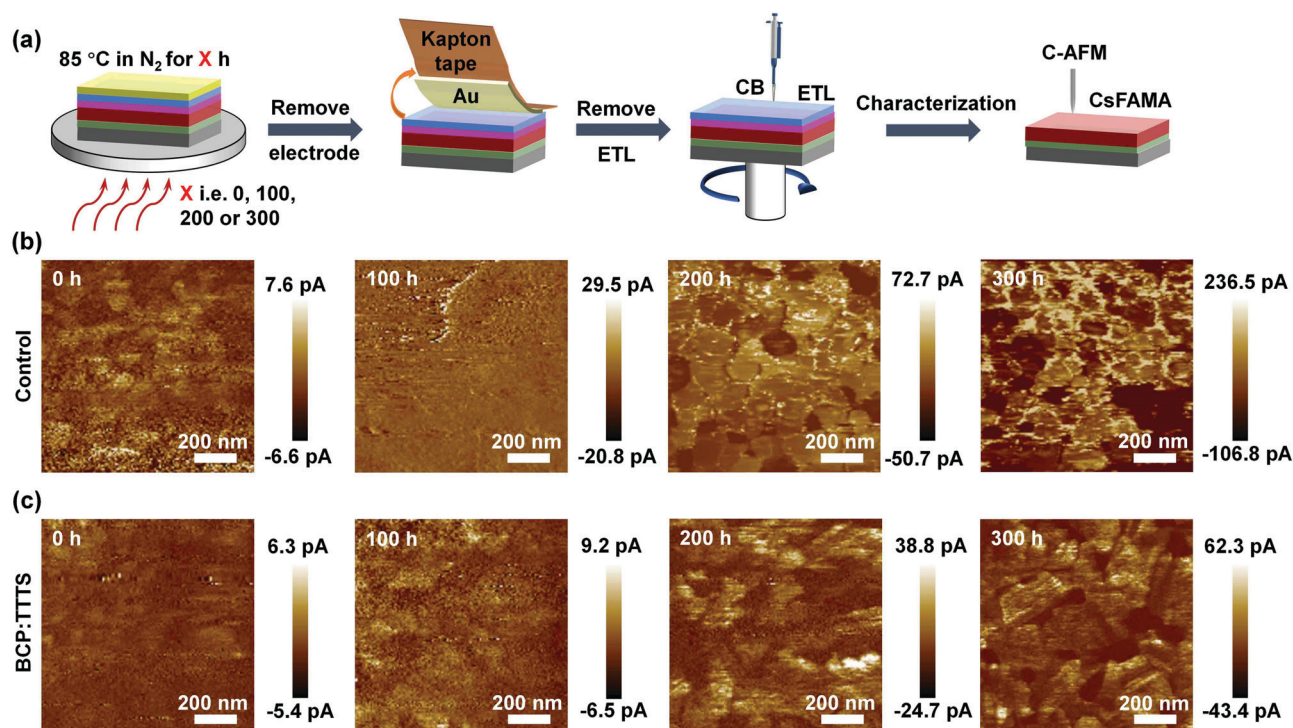

Fig. 5 C-AFM images of perovskite films after the top Au electrode and ETL were stripped. (a) The preparation process of perovskite films for C-AFM characterization. C-AFM images of perovskite films obtained from the PSCs (b) without and (c) with TTTS after different heating times (*i.e.*, 0, 100, 200 and 300 h) at 85 °C in an N$_2$-filled glovebox. All C-AFM images were obtained under an applied bias of 1 V on the perovskite films. CB is chlorobenzene.

To observe the vertical distribution of Au, we conducted cross-sectional scanning transmission electron microscopy (STEM) and EDX spectroscopy. The STEM images and EDX mapping were obtained from the shaped devices *via* focused
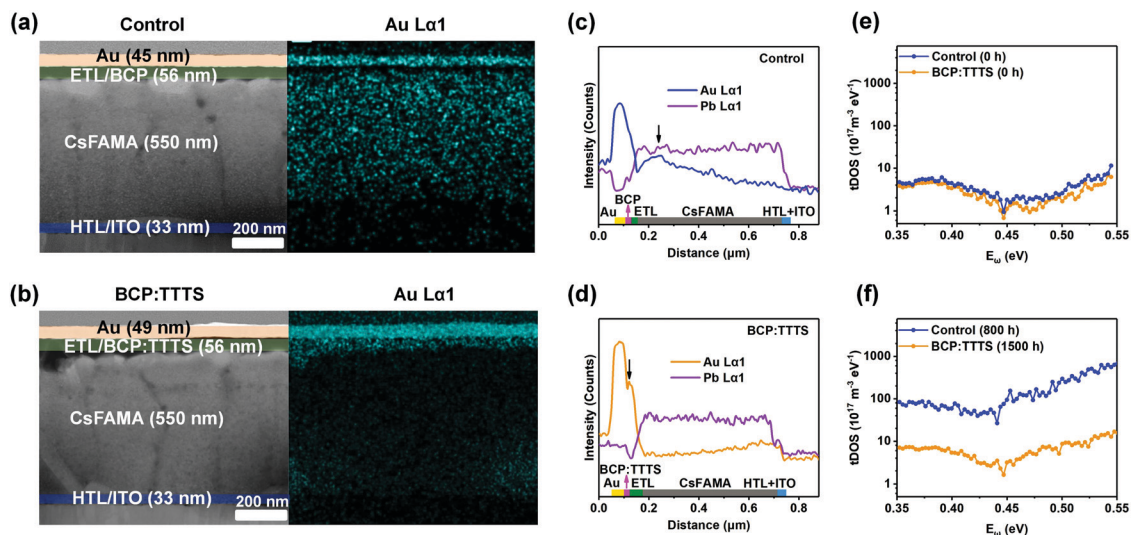
This journal is © The Royal Society of Chemistry 2022

Energy Environ. Sci., 2022, **15**, 2154–2163 | **2159**

Fig. 6 STEM and tDOS characterization of the devices. Cross-sectional STEM analysis and the corresponding EDX mapping of the Au element for the aged devices (a) without and (b) with TTTS. Corresponding line-scanning profiles of the devices (c) without and (d) with TTTS. The inset is the regional distribution of each functional layer in the PSCs. tDOS curves of the control and BCP:TTTS devices (e) before and (f) after the thermal stability test.

ion beam (FIB) before (Fig. S14, ESI†) and after (Fig. 6(a) and (b)) accelerated aging at 85 °C in an N_2-filled glovebox for 300 h. The perovskite active layer and Au electrode, separated by an ETL can be clearly observed in the STEM images. We measured the thickness of the layers for the fresh and aged devices, where the thickness of Au (50 nm) was basically the same for the BCP:TTTS device before and after aging; however, it was reduced from 50 nm to 45 nm for the control device, suggesting that a large amount of Au strayed from the electrode region. The EDX mapping also shows that a significant Au signal can be observed throughout the perovskite layer for the control device (Fig. 6(a)), which indicates Au migration through the whole perovskite layer.[51] On the contrary, the Au signal is only obviously observed in the ETL for the BCP:TTTS device (Fig. 6(b)) owing to the strong interaction between Au and TTTS, which inhibited its further migration to the perovskite layer. This was also confirmed by the line-scanning profiles, as shown in Fig. 6(c) and (d).

The inward diffusion of Au into the perovskite layer may cause deep-level defects as effective recombination centers, resulting in the deterioration of the stability of PSCs.[29] Therefore, we employed the trap density of states (tDOS) to investigate the effect of TTTS on the defect density of the devices before and after the thermal stability test. We calculated the tDOS using the following equation:[52]

$$N_T(E_\omega) = -\frac{V_{bi}}{qW}\frac{dC}{d\omega}\frac{\omega}{k_B T} \qquad (1)$$

where C is the capacitance, W is the depletion width, k_B is the Boltzmann constant and q is the electron charge. V_{bi} is the built-in potential obtained from the Mott–Schottky plot (Fig. S15, ESI†), and E_ω is the energy demarcation calculated from

the applied angular frequency (ω) according to the following equation:[52]

$$E_\omega = k_B T \ln\frac{\omega_0}{\omega} \qquad (2)$$

where ω_0 is the attempt-to-escape frequency. Before the stability test, the tDOS values of the BCP:TTTS device were similar to that of the control device, as shown in Fig. 6(e). After the stability test (Fig. 6(f)), the tDOS values of the BCP:TTTS device exhibited no obvious change compared to that before the stability test. In contrast, a significant increase in the tDOS was observed for the control device after the stability test, indicating the presence of more defects caused by the diffusion of Au.

To verify the universality of the TTTS additive strategy, we studied other common metal electrodes such as Cu and Ag. TTTS also has strong interaction with Cu (Ag) as it is attached to Au. J–V characterization (Fig. 7(a) and (b)), operational stability (Fig. 7(c) and (d)) and thermal stability (Fig. 7(e) and (f)) tests were performed. The BCP:TTTS device with Cu electrode showed an improved PCE of 21.31% from 19.11% (control device) (Table S6, ESI†). Similarly, the PCE of the BCP:TTTS device with the Ag electrode was enhanced from 19.66% (control device) to 21.53% (Table S7, ESI†). This directly reveals that the TTTS additive strategy is universal for improving the device efficiency. Moreover, the optimized encapsulated champion devices with the Cu or Ag electrode maintained 97% or 96% of their initial SPO after MPP tracking and continuous illumination at 45 °C after 1000 h, respectively. In addition, the optimized unencapsulated BCP:TTTS devices with the Cu and Ag electrodes showed excellent thermal stability, maintaining 94% and 91% (average PCE from ten devices) of their initial PCE values at 85 °C in an N_2-filled glovebox after 1500 h,
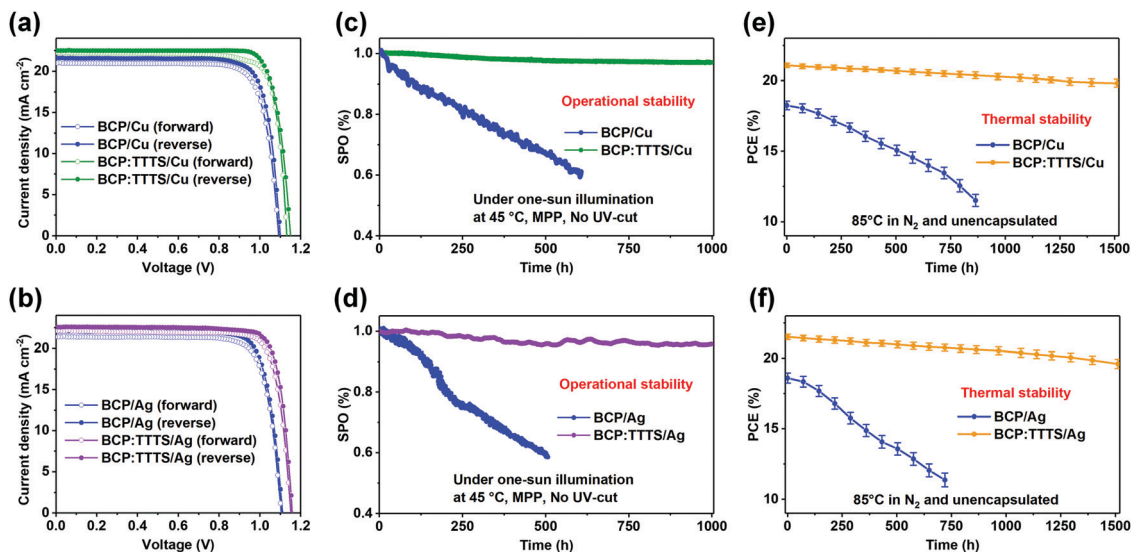
2160 | *Energy Environ. Sci.*, 2022, **15**, 2154–2163

This journal is © The Royal Society of Chemistry 2022

Fig. 7 *J–V* curves and stability characterization of the control and BCP:TTTS devices with different electrodes. *J–V* curves of the devices with (a) Cu and (b) Ag electrodes. The scan rate was 0.1 V s^{-1}. Operational stability with (c) Cu and (d) Ag electrodes. The operational stability test of the encapsulated devices was conducted under one-sun illumination without a UV (ultraviolet) filter at 45 °C to track the MPP. The SPO traces are the degradation of a single champion device for the control and BCP:TTTS devices. Thermal stability devices with (e) Cu and (f) Ag electrodes. The thermal stability test of the unencapsulated devices was performed at 85 °C in an N$_2$-filled glovebox. The average PCE and standard error were calculated from ten devices.

respectively. For the scaling up of PSCs, Ag paste may be applied during the preparation of the perovskite cells.[53] Therefore, we selected Ag paste as the electrode and prepared PSCs for the operational stability test, as shown in Fig. S16 (ESI†). The SPO value of the modified device with TTTS was maintained at 93% compared with that of the control device (62%) after 500 h continuous illumination at 45 °C. We also introduced TTTS in conventional PSCs.[54] As shown in Fig. S17 and S18 (ESI†), the modified device with TTTS displays an enhanced PCE from 19.45% (control device) to 22.13%, and its champion SPO after 500 h was still maintained at 92% compared with the control device (68%) in the operational stability test. Thus, these results indicate the universality of the blocking effect for TTTS additive to Cu and Ag.

3. Conclusions

We employed TTTS as a multifunctional additive to inhibit metal-inward diffusion-induced degradation toward stable and efficient inverted perovskite solar cells. Different from the physical separation barriers, the TTTS additive blocked the inward diffusion of the metal electrode (Au, Cu, and Ag) through strong chemical coordination, leading to a significantly improved device stability, including operational, ambient, and thermal stabilities. The optimized champion devices exhibited almost no loss in their initial efficiency at the MPP under continuous one-sun light soaking for 1000 h, 91% (average PCE from ten devices) in air (50% ± 5% RH) at 25 °C for 5000 h, and 93% (average PCE from ten devices) after heating at 85 °C in N$_2$ for 1500 h. In addition, TTTS can adjust the band structure of BCP, enhance electron extraction and transport, and thus reduce carrier recombination. The

champion BCP:TTTS device achieved an exciting PCE of 22.59%, which is among the highest PCEs for inverted PSCs. Our study provides an effective and universal additive engineering strategy to prevent the inward diffusion of the metal electrode without sacrificing the efficiency.

Author contributions

J. B. Yang performed the overall experiments and wrote the original manuscript. Q. Cao and T. Wang contributed to the fabrication of perovskite solar cell and revision of the manuscript. X. Y. Pu, Y. X. Zhang and H. Chen helped the optimization and characterizations of devices. X. H. Li supervised the work. Y. K. Li, L. Etgar, I. Tojiboyev, B. W. Yang, and A. Hagfeldt contributed to revision of the manuscript.

Conflicts of interest

The authors declare no conflict of interest.

Acknowledgements

References

1 J. Jeong, M. Kim, J. Seo, H. Lu, P. Ahlawat, A. Mishra, Y. Yang, M. A. Hope, F. T. Eickemeyer, M. Kim, Y. J. Yoon, I. W. Choi, B. P. Darwich, S. J. Choi, Y. Jo, J. H. Lee, B. Walker, S. M. Zakeeruddin, L. Emsley, U. Rothlisberger, A. Hagfeldt, D. S. Kim, M. Grätzel and J. Y. Kim, *Nature*, 2021, **592**, 381–385.

2 Q. Cao, Y. Li, H. Zhang, J. Yang, J. Han, T. Xu, S. Wang, Z. Wang, B. Gao, J. Zhao, X. Li, X. Ma, S. M. Zakeeruddin, W. E. I. Sha, X. Li and M. Grätzel, *Sci. Adv.*, 2021, **7**, eabg0633.

3 Q. Cao, J. Yang, T. Wang, Y. Li, X. Pu, J. Zhao, Y. Zhang, H. Zhou, X. Li and X. Li, *Energy Environ. Sci.*, 2021, **14**, 5406–5415.

4 L. Jia, F. Huang, H. Ding, C. Niu, Y. Shang, W. Hu, X. Li, X. Yu, X. Jiang, R. Cao, J. Zhu, G.-W. Wang, M. Chen and S. Yang, *Nano Today*, 2021, **39**, 101164.

5 T. Li, S. Wang, J. Yang, X. Pu, B. Gao, Z. He, Q. Cao, J. Han and X. Li, *Nano Energy*, 2021, **82**, 105742.

6 S. Wang, Z. Li, Y. Zhang, X. Liu, J. Han, X. Li, Z. Liu, S. Liu and W. C. H. Choy, *Adv. Funct. Mater.*, 2019, **29**, 1900417.

7 Q. Cao, Z. Li, J. Han, S. Wang, J. Zhu, H. Tang, X. Li and X. Li, *Sol. RRL*, 2019, **3**, 1900333.

8 S. Guo, X. Sun, C. Ding, R. Huang, M. Tan, L. Zhang, Q. Luo, F. Li, J. Jin and C.-Q. Ma, *Energy Technol.*, 2020, **8**, 2000250.

9 H. Choi, X. Liu, H. I. Kim, D. Kim, T. Park and S. Song, *Adv. Energy Mater.*, 2021, **11**, 2003829.

10 M. Stolterfoht, C. M. Wolff, J. A. Márquez, S. Zhang, C. J. Hages, D. Rothhardt, S. Albrecht, P. L. Burn, P. Meredith, T. Unold and D. Neher, *Nat. Energy*, 2018, **3**, 847–854.

11 J.-H. Kim, Y. R. Kim, B. Park, S. Hong, I.-W. Hwang, J. Kim, S. Kwon, G. Kim, H. Kim and K. Lee, *Small*, 2020, **17**, 2005608.

12 Q. Li, Y. Dong, G. Lv, T. Liu, D. Lu, N. Zheng, X. Dong, Z. Xu, Z. Xie and Y. Liu, *ACS Energy Lett.*, 2021, **6**, 2072–2080.

13 X. Zheng, Y. Hou, C. Bao, J. Yin, F. Yuan, Z. Huang, K. Song, J. Liu, J. Troughton, N. Gasparini, C. Zhou, Y. Lin, D.-J. Xue, B. Chen, A. K. Johnston, N. Wei, M. N. Hedhili, M. Wei, A. Y. Alsalloum, P. Maity, B. Turedi, C. Yang, D. Baran, T. D. Anthopoulos, Y. Han, Z.-H. Lu, O. F. Mohammed, F. Gao, E. H. Sargent and O. M. Bakr, *Nat. Energy*, 2020, **5**, 131–140.

14 S. Wang, Z. Zhang, Z. Tang, C. Su, W. Huang, Y. Li and G. Xing, *Nano Energy*, 2021, **82**, 105712.

15 J. Han, S. Wang, J. Yang, S. Guo, Q. Cao, H. Tang, X. Pu, B. Gao and X. Li, *ACS Appl. Mater. Interfaces*, 2020, **12**, 4970–4979.

16 H. Zhou, J. Han, X. Pu and X. Li, *J. Materiomics*, 2021, **7**, 1074–1082.

17 X. Xin, Y. Song, S. Guo, Y. Zhang, B. Wang, J. Yu and X. Li, *Appl. Catal., B*, 2020, **269**, 118773.

18 B. Wang, S. Guo, X. Xin, Y. Zhang, Y. Wang, C. Li, Y. Song, D. Deng, X. Li, A. J. Sobrido and M.-M. Titirici, *Adv. Energy Mater.*, 2020, **10**, 2001575.

19 S. Wang, X. Li, T. Tong, J. Han, Y. Zhang, J. Zhu, Z. Huang and W. C. H. Choy, *Sol. RRL*, 2018, **2**, 1800027.

20 S. Chen, X. Dai, S. Xu, H. Jiao, L. Zhao and J. Huang, *Science*, 2021, **373**, 902–907.

21 F. Li, X. Deng, F. Qi, Z. Li, D. Liu, D. Shen, M. Qin, S. Wu, F. Lin, S.-H. Jang, J. Zhang, X. Lu, D. Lei, C.-S. Lee, Z. Zhu and A. K. Y. Jen, *J. Am. Chem. Soc.*, 2020, **142**, 20134–20142.

22 N. Li, X. Niu, Q. Chen and H. Zhou, *Chem. Soc. Rev.*, 2020, **49**, 8235–8286.

23 P. Guo, Q. Ye, C. Liu, F. Cao, X. Yang, L. Ye, W. Zhao, H. Wang, L. Li and H. Wang, *Adv. Funct. Mater.*, 2020, **30**, 2002639.

24 S. Guo, Y. Li, S. Tang, Y. Zhang, X. Li, A. J. Sobrido, M.-M. Titirici and B. Wei, *Adv. Funct. Mater.*, 2020, **30**, 2003035.

25 D. B. Khadka, Y. Shirai, M. Yanagida and K. Miyano, *ACS Appl. Mater. Interfaces*, 2019, **11**, 7055–7065.

26 S. Zhang, Z. Liu, W. Zhang, Z. Jiang, W. Chen, R. Chen, Y. Huang, Z. Yang, Y. Zhang, L. Han and W. Chen, *Adv. Energy Mater.*, 2020, **10**, 2001610.

27 K. Domanski, J.-P. Correa-Baena, N. Mine, M. K. Nazeeruddin, A. Abate, M. Saliba, W. Tress, A. Hagfeldt and M. Grätzel, *ACS Nano*, 2016, **10**, 6306–6314.

28 C. C. Boyd, R. Cheacharoen, K. A. Bush, R. Prasanna, T. Leijtens and M. D. McGehee, *ACS Energy Lett.*, 2018, **3**, 1772–1778.

29 W. Ming, D. Yang, T. Li, L. Zhang and M.-H. Du, *Adv. Sci.*, 2018, **5**, 1700662.

30 L. Liu, S. Huang, Y. Lu, P. Liu, Y. Zhao, C. Shi, S. Zhang, J. Wu, H. Zhong, M. Sui, H. Zhou, H. Jin, Y. Li and Q. Chen, *Adv. Mater.*, 2018, **30**, 1800544.

31 Z. Yang, B. H. Babu, S. Wu, T. Liu, S. Fang, Z. Xiong, L. Han and W. Chen, *Sol. RRL*, 2019, **4**, 1900257.

32 S. Bai, P. Da, C. Li, Z. Wang, Z. Yuan, F. Fu, M. Kawecki, X. Liu, N. Sakai, J. T. Wang, S. Huettner, S. Buecheler, M. Fahlman, F. Gao and H. J. Snaith, *Nature*, 2019, **571**, 245–250.

33 X. Dong, X. Fang, M. Lv, B. Lin, S. Zhang, J. Ding and N. Yuan, *J. Mater. Chem. A*, 2015, **3**, 5360–5367.

34 J. A. Christians, P. Schulz, J. S. Tinkham, T. H. Schloemer, S. P. Harvey, B. J. Tremolet de Villers, A. Sellinger, J. J. Berry and J. M. Luther, *Nat. Energy*, 2018, **3**, 68–74.

35 M. Liu, Z. Chen, Y. Yang, H.-L. Yip and Y. Cao, *J. Mater. Chem. A*, 2019, **7**, 17324–17333.

36 Z. Jiang, X. Chen, X. Lin, X. Jia, J. Wang, L. Pan, S. Huang, F. Zhu and Z. Sun, *Sol. Energy Mater. Sol. Cells*, 2016, **146**, 35–43.

37 J. Zhao, K. O. Brinkmann, T. Hu, N. Pourdavoud, T. Becker, T. Gahlmann, R. Heiderhoff, A. Polywka, P. Görrn, Y. Chen, B. Cheng and T. Riedl, *Adv. Energy Mater.*, 2017, **7**, 1602599.

38 V.-D. Tran, S. V. N. Pammi, B.-J. Park, Y. Han, C. Jeon and S.-G. Yoon, *Nano Energy*, 2019, **65**, 104018.

39 J. Yang, Q. Cao, Z. He, X. Pu, T. Li, B. Gao and X. Li, *Nano Energy*, 2021, **82**, 105731.

40 Y. Kim, G. Kim, N. J. Jeon, C. Lim, J. Seo and B. J. Kim, *ACS Energy Lett.*, 2020, **5**, 3304–3313.

41 Y. Dong, D. Lu, Z. Xu, H. Lai and Y. Liu, *Adv. Energy Mater.*, 2020, **10**, 2000694.

42 C. Hu, Y. Bai, S. Xiao, K. Tao, W. K. Ng, K. S. Wong, S. H. Cheung, S. K. So, Q. Chen and S. Yang, *Sol. RRL*, 2020, **4**, 2000270.

43 M. Ikai, S. Tokito, Y. Sakamoto, T. Suzuki and Y. Taga, *Appl. Phys. Lett.*, 2001, **79**, 156–158.

44 R. Chadha, A. Das, A. K. Debnath, S. Kapoor and N. Maiti, *Colloids Surf., A*, 2021, **615**, 126279.

45 N. Arisnabarreta, G. D. Ruano, M. Lingenfelder, E. M. Patrito and F. P. Cometto, *Langmuir*, 2017, **33**, 13733.

46 M. S. Tyler, M. Walker and R. A. Hatton, *ACS Appl. Mater. Interfaces*, 2016, **8**, 12316–12323.

47 C.-Y. Chang, Y.-C. Chang, W.-K. Huang, W.-C. Liao, H. Wang, C. Yeh, B.-C. Tsai, Y.-C. Huang and C.-S. Tsao, *J. Mater. Chem. A*, 2016, **4**, 7903–7913.

48 N. Chakravarthi, K. Gunasekar, W. Cho, D. X. Long, Y.-H. Kim, C. E. Song, J.-C. Lee, A. Facchetti, M. Song, Y.-Y. Noh and S.-H. Jin, *Energy Environ. Sci.*, 2016, **9**, 2595–2602.

49 J. Zhao, X. Zheng, Y. Deng, T. Li, Y. Shao, A. Gruverman, J. Shield and J. Huang, *Energy Environ. Sci.*, 2016, **9**, 3650–3656.

50 S. Hong, J. Lee, H. Kang, G. Kim, S. Kee, J.-H. Lee, S. Jung, B. Park, S. Kim, H. Back, K. Yu and K. Lee, *Sci. Adv.*, 2018, **4**, eaat3604.

51 R. Wang, J. Xue, L. Meng, J.-W. Lee, Z. Zhao, P. Sun, L. Cai, T. Huang, Z. Wang, Z.-K. Wang, Y. Duan, J. L. Yang, S. Tan, Y. Yuan, Y. Huang and Y. Yang, *Joule*, 2019, **3**, 1464–1477.

52 N. Li, S. Tao, Y. Chen, X. Niu, C. K. Onwudinanti, C. Hu, Z. Qiu, Z. Xu, G. Zheng, L. Wang, Y. Zhang, L. Li, H. Liu, Y. Lun, J. Hong, X. Wang, Y. Liu, H. Xie, Y. Gao, Y. Bai, S. Yang, G. Brocks, Q. Chen and H. Zhou, *Nat. Energy*, 2019, **4**, 408–415.

53 Y. Y. Kim, T.-Y. Yang, R. Suhonen, M. Välimäki, T. Maaninen, A. Kemppainen, N. J. Jeon and J. Seo, *Adv. Sci.*, 2019, **6**, 1802094.

54 Y. Y. Kim, T.-Y. Yang, R. Suhonen, A. Kemppainen, K. Hwang, N. J. Jeon and J. Seo, *Nat. Commun.*, 2020, **11**, 5146.

This journal is © The Royal Society of Chemistry 2022

Energy Environ. Sci., 2022, **15**, 2154–2163 | **2163**